Engineering xxx (xxxx) xxx

Contents lists available at ScienceDirect

Engineering

journal homepage: www.elsevier.com/locate/eng

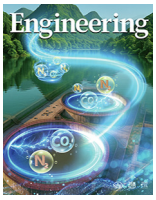

Research
Nuclear Power—Article

Anti-Polyelectrolyte-Effect Hydrogel Unlocks Efficient Uranium Extraction from Concentrated Seawater

Hui Wang [a], Feng Gao [a], Taohong Xu [a], Peng Liu [a], Zhanhu Guo [b], Guanbing Zhou [a,*], Yihui Yuan [a,*], Ning Wang [a,*]

[a] State Key Laboratory of Marine Resource Utilization in South China Sea, Hainan University, Haikou 570228, China
[b] Department of Mechanical & Construction Engineering, Northumbria University, Newcastle Upon Tyne NE1 8ST, UK

ARTICLE INFO

Article history:
Received 21 September 2025
Revised 11 November 2025
Accepted 26 November 2025
Available online xxxx

Keywords:
Uranium extraction
Concentrated seawater
Anti-polyelectrolyte effect
Functional group accessibility
Anti-biofouling

ABSTRACT

Uranium extraction from seawater is a promising strategy to alleviate global uranium scarcity, yet its implementation is hindered by extremely low concentrations and complex ionic environments. Concentrated seawater brine, a byproduct of salt production and desalination, contains 2–10 times more uranium than natural seawater, yet its high salinity presents additional challenges for extraction. Conventional polyamidoxime (PAO) hydrogels exhibit salt-induced shrinkage, compromising functional group accessibility and adsorption efficiency. Herein, we develop an anti-polyelectrolyte effect hydrogel by composing polyvinylphosphonic acid (PVPA) and the PAO. Under high-salinity conditions, cations and anions accumulate via diffusion around the positively charged amidoxime and negatively charged phosphonic acid groups, weakening interchain electrostatic attractions. This anti-polyelectrolyte effect promotes hydrogel swelling, significantly improving the exposure of binding sites and uranyl ion uptake. The PVPA–PAO hydrogel achieves a uranium adsorption capacity of 43.89 $mg{\cdot}g^{-1}$ after 24 days in concentrated natural seawater derived from solar saltworks, significantly surpassing that of previously reported PAO hydrogels (~10 $mg{\cdot}g^{-1}$). In addition, it exhibits excellent antibacterial performance, mechanical robustness, and ion selectivity. This work presents an effective strategy for improving uranium recovery from marine resources and advances the comprehensive development and utilization of seawater resources.

1. Introduction

Global warming highlights the urgent need to cut carbon emissions and ensure sustainable development [1]. Fossil fuels are not only limited in reserves but also lead to serious environmental problems, while clean energies such as wind and solar are constrained by intermittency [2–4]. In this context, nuclear energy, with high energy density and low carbon emissions, represents a promising alternative [5]. However, the finite nature and gradual depletion of terrestrial uranium resources, coupled with the environmental burdens associated with conventional mining, pose significant constraints on the long-term sustainability of nuclear energy [6,7]. The ocean contains an estimated 4.5 billion tons of uranium, approximately 1000 times the amount found in terrestrial ores, offering a virtually inexhaustible alternative resource [8,9]. Extracting uranium from seawater holds the potential to fundamentally alleviate the constraints imposed by limited land-based supplies and to ensure the sustainable development of nuclear energy [10,11]. Nevertheless, the practical implementation of seawater uranium extraction faces considerable challenges, including the extremely low concentration of uranium (~3 parts per billion (ppb)), the presence of a wide range of competing ions, and the severe degradation of adsorbent performance due to biofouling [12–14]. Research now centers on materials and systems that efficiently extract uranium in real environment, advancing technical feasibility and long-term sustainability [15,16].

Notably, concentrated seawater produced continuously during solar saltworks and seawater desalination operations exhibit uranium concentrations ranging from 2 to 10 times those of natural seawater. Integrating uranium extraction technologies with these

* Corresponding authors.
E-mail addresses: zhouguanbing@hainanu.edu.cn (G. Zhou), yuanyh@hainanu.edu.cn (Y. Yuan), wangn02@foxmail.com (N. Wang).

https://doi.org/10.1016/j.eng.2025.11.024

Please cite this article as: H. Wang, F. Gao, T. Xu et al., Anti-Polyelectrolyte-Effect Hydrogel Unlocks Efficient Uranium Extraction from Concentrated Seawater, Engineering, https://doi.org/10.1016/j.eng.2025.11.024

existing industrial processes offers a promising route to enhance extraction efficiency and reduce operational costs [17,18]. Although uranium concentrations in concentrated seawater are substantially elevated, their complex physicochemical environments, characterized by high salinity and pronounced electrostatic effects, pose significant technical challenges. Macroscopic polyamidoxime (PAO)-based hydrogel adsorbents are among the most promising candidates for large-scale uranium extraction from seawater, owing to the strong uranyl-binding affinity of amidoxime groups and the excellent structural robustness of the polymeric network [19,20]. In marine environments, amidoxime groups bear anionic character; under high-salinity conditions, they become increasingly surrounded by cations, particularly Na^+, which screen electrostatic repulsion and induce polymer chain contraction. This phenomenon, commonly referred to as salt shrinkage, causes the originally porous hydrogel network to collapse, thereby reducing mass transport efficiency and limiting the accessibility of active binding sites [21,22]. Consequently, adsorption performance deteriorates markedly [23]. Furthermore, biofouling resulting from microbial colonization on adsorbent surfaces further diminishes adsorption capacity and shortens material lifespan [24,25]. Therefore, the development of advanced adsorbents that maintain high uranyl affinity, structural integrity, and anti-fouling properties under extreme saline conditions is critical for the practical implementation of uranium extraction from concentrated seawater sources, such as those generated by seawater solar saltworks and desalination.

To address these limitations, significant efforts have been devoted to developing next-generation adsorbents with enhanced resistance to salt shrinkage and biofouling [26,27]. Strategies such as introducing hydrophilic functional groups and stabilizing surface charge distributions have proven effective in mitigating salt-induced performance degradation [28]. However, these approaches have so far only demonstrated salt shrinkage mitigation in normal seawater conditions, with no reports detailing their performance in highly concentrated seawater. Meanwhile, the incorporation of antibacterial components into adsorbent materials has shown promise in preventing microbial adhesion and biofilm formation [29]. Nevertheless, most antibacterial moieties lack specific affinity toward uranyl ions, and excessive addition of antibacterial agents can occupy uranyl adsorption sites, which is detrimental to both adsorption capacity and economic viability. Polyvinylphosphonic acid (PVPA), containing phosphonic acid groups, exhibits both strong uranyl-binding capacity and anti-biofouling properties due to its hydrophilic and anti-adhesive characteristics [30,31]. Furthermore, polyelectrolyte composites, characterized by dissociable ionic groups along their polymer chains, display a unique anti-polyelectrolyte effect [32,33] under high-salinity conditions, transitioning from collapsed to extended chain conformations, thereby exposing more active sites for adsorption.

Herein, we report a rationally designed polyelectrolyte composite hydrogel composed of PVPA and PAO, tailored to overcome salt-induced collapse and biofouling in uranium extraction from high-salinity brines (Fig. 1). The hydrogel network is physically cross-linked through electrostatic interactions between oppositely charged polyelectrolyte segments. Under high-salinity conditions, counterions in the brine weaken internal electrostatic attractions, driving the polymer chain to transition from a collapsed to an extended conformation with increased inter-chain spacing. This typical anti-polyelectrolyte effect induces salt-triggered swelling, which greatly enhances the exposure and accessibility of uranyl-binding functional groups, thereby improving adsorption performance. Additionally, the incorporation of PVPA imparts inherent anti-biofouling properties and improves long-term material stability under saline conditions. After 24 days of immersion in concentrated seawater derived from solar saltworks, the PVPA–PAO hydrogel achieved a uranium adsorption capacity of 43.89 $mg \cdot g^{-1}$, significantly outperforming previously reported PAO hydrogels ($\sim$10 $mg \cdot g^{-1}$). It also exhibited a high antibacterial rate of 99.94%, and its adsorption capacity in open seawater decreased by only 6.29% compared to filtered seawater. Moreover, the hydrogel demonstrated excellent ion selectivity and mechanical robustness, highlighting its potential for practical deployment in uranium recovery from concentrated seawater. Beyond addressing key technical challenges in concentrated natural seawater brine-based uranium extraction, this work also reflects a broader shift toward the synergistic development and utilization of multiple seawater-derived resources, such as salt, water, and uranium, thereby enhancing resource utilization efficiency and added value.

2. Materials and methods

2.1. Materials

Hydroxylamine hydrochloride ($NH_2OH \cdot HCl$, 98.5%), polyacrylonitrile (PAN; weight-average molecular weight (M_w) = 150 000, 99%), and Arsenazo III (95%) were purchased from Macklin Reagent Co., Ltd. (China). Sodium carbonate (Na_2CO_3, 97.5%), dimethylformamide (DMF; 99%), sodium hydroxide (NaOH, 98.5%), sodium chloride (NaCl, 99.5%), ammonium persulfate (APS, 98%), hydrochloric acid (12 $mol \cdot L^{-1}$), and anhydrous ethanol were purchased from Xilong Scientific Co. Ltd. (China). Vinylphosphonic acid (VPA, 95%) was purchased from Aladdin Biochemical Technology Co., Ltd. (China). Uranyl hexahydrate nitrate ($UO_2(NO_3)_2 \cdot 6H_2O$, 99%) was purchased from Chushengwei Chemical Co., Ltd. (China). Concentrated seawater was obtained from Yinggehai Salt Field, Hainan Province, China. Unless otherwise noted, all reagents were used as received.

2.2. Preparation of materials

Preparation of PAO. In a typical run, 5.6 g of $NH_2OH \cdot HCl$ was dissolved in 60 mL of DMF at 45 °C. Then, 1.6 g of NaOH and 4.12 g of Na_2CO_3 were added to the solution, followed by stirring at 45 °C for 1 h. Next, 4 g of PAN was slowly added to the solution and allowed to fully dissolve over 15 min, after which the temperature was increased to 65 °C. After 24 h, 30 mL of DMF was added to the reaction flask, followed by 2.8 g of $NH_2OH \cdot HCl$, which was fully dissolved. After 15 min, 0.8 g of NaOH and 2.06 g of Na_2CO_3 were added successively to the reaction flask, and the reaction continued at 65 °C for an additional 24 h. Finally, the reaction mixture was transferred to centrifuge tubes and centrifuged at 11000 revolutions per minute (rpm) for 25 min. The supernatant was then slowly added to 1000 mL of absolute ethanol to precipitate a white granule while stirring. After 12 h, the precipitate was collected by suction filtration and dried in a vacuum oven at 40 °C for 12 h to obtain the as-prepared PAO.

Preparation of PVPA–PAO composite hydrogel. The PVPA–PAO composite hydrogel was prepared via free radical polymerization. First, 1.137 g of VPA (95%) was dissolved in 10 mL of deionized water with stirring under ice–water bath conditions. After complete dissolution, 1.722 g of PAO was added and fully dispersed by vortexing. Subsequently, 0.5 mL of 50 $mg \cdot mL^{-1}$ APS solution was introduced to initiate the polymerization. The mixture was homogenized and cast into a mold, followed by polymerization in an oven at 60 °C for 6 h. After curing, the hydrogel was removed from the mold and thoroughly washed with deionized water to remove unreacted monomers and impurities.

2.3. Characterization

The conventional microstructures of the adsorbents were analyzed using a scanning electron microscope (Axia ChemiSEM,

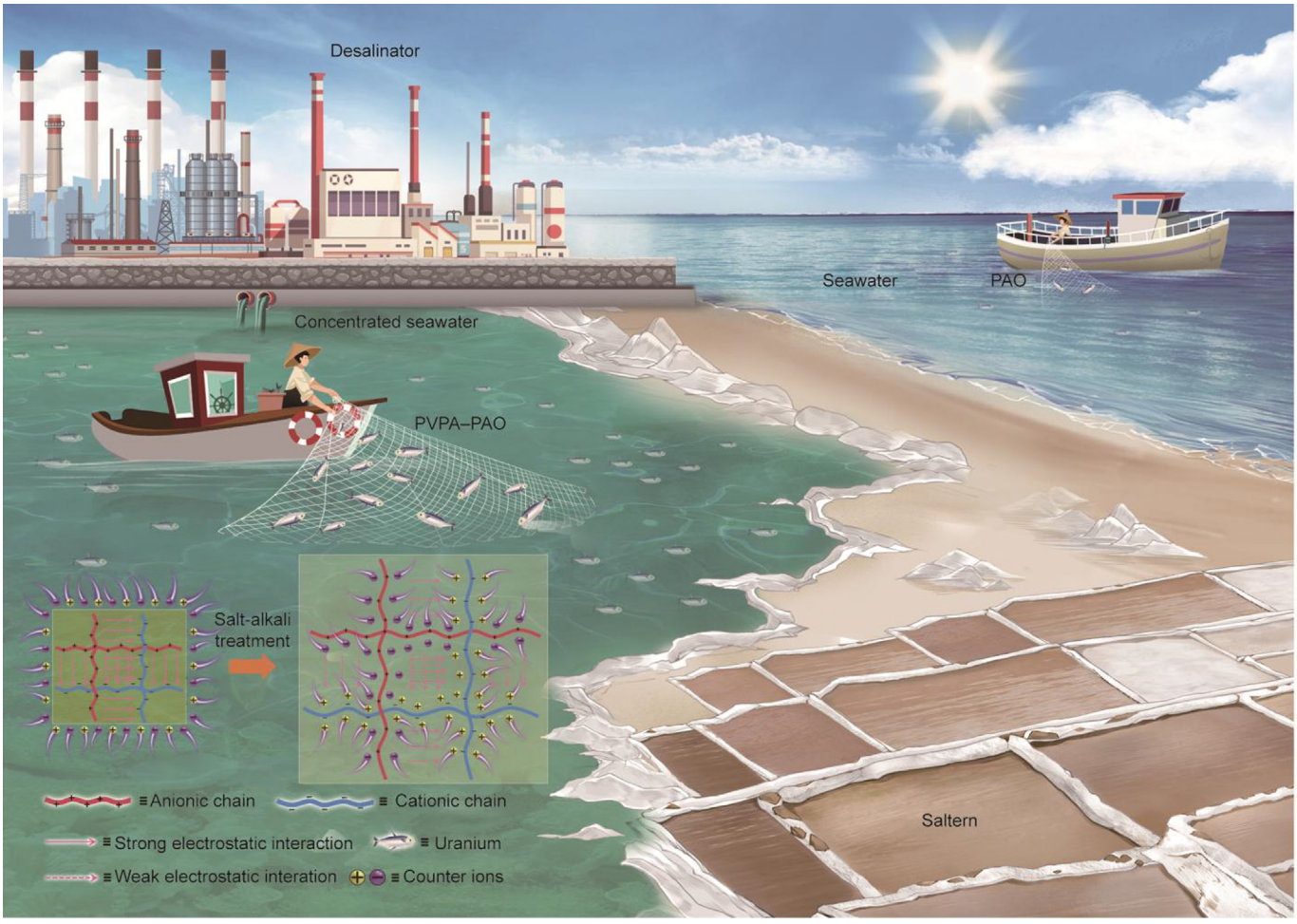

Fig. 1. Schematic illustration of PVPA–PAO application for uranium extraction from concentrated seawater generated by seawater desalination and solar saltworks.

Thermo Fisher Scientific, USA). The swollen microstructures were observed with an environmental scanning electron microscope (ESEM; QUANTA200). Surface functional groups were characterized by Fourier-transform infrared (FT-IR) spectroscopy (Nicolet 6700, Thermo Fisher Scientific) within the 400–4000 cm^{-1} range, with the sample prepared as a pressed KBr pellet (1 wt% of dry gel mixed with KBr). Raman spectroscopy (Renishaw inVia, Gloucestershire, UK) was also used to study the surface functional groups of the adsorbent. The specific surface area was determined through nitrogen (N_2) adsorption-desorption isotherms at 77 K using a Brunauer–Emmett–Teller (BET) analyzer (TriStar II 3020, Micromeritics, USA). The Zeta potential of PVPA–PAO was measured within the pH range of 3.00–9.00 using a Zetasizer Nano analyzer (ZS90, Malvern Instruments Inc., UK). Elemental chemical states were determined by X-ray photoelectron spectroscopy (XPS; Escalab 250Xi, Thermo Electron Corporation, USA), with high-resolution spectral binding energy analysis. Additionally, N_2 adsorption–desorption isotherms were conducted with a Micromeritics ASAP 2460 analyzer to evaluate the specific surface area of the adsorbents. Uranium and competitive metal ion concentrations were measured using a ultraviolet-visible (UV-Vis) spectrophotometer (UV1800PC, Shanghai Jinghua Instruments Co., Ltd., China), inductively coupled plasma optical emission spectrometry (ICP-OES; 725ES, Agilent, USA), and inductively coupled plasma mass spectrometry (ICP-MS, 7800, Agilent). Tensile testing of the adsorbents was performed using a universal tensile-compressive machine (CMT 6503, MTS Systems China Co. Ltd.).

2.4. Antibacterial experiments

To evaluate the antibacterial properties of the samples, experiments were conducted to investigate their effect on bacterial growth and inhibition. For the preparation of Luria-Bertani (LB) liquid medium, 100 mL of distilled water was measured and transferred into a 250 mL reagent bottle, followed by the addition of 2.5 g of LB broth. The mixture was thoroughly mixed and then sterilized by autoclaving at 121 °C for 15 min. For LB solid medium, 100 mL of distilled water was measured into a 250 mL reagent bottle, and 2.5 g of LB broth and 1.5 g of agar powder were added and mixed thoroughly. The mixture was autoclaved at 121 °C for 15 min. After cooling to approximately 40–50 °C, 15 mL of the medium was transferred into a sterile Petri dish. To enrich the bacterial suspension, the sample concentrated natural seawater brine solution was mixed with the LB solution in a 1:1 ratio and incubated at 28 °C with shaking for 48 h. Enrichment was complete when the solution became turbid. The enriched bacterial suspension was then diluted to 10^6 colony-forming unit (CFU)·mL^{-1} with PBS. A 200 mg sample was weighed and combined with 2 mL of the diluted bacterial suspension, resulting in a final concentration of 100 mg·mL^{-1}. The mixture was incubated at 28 °C for 24 h, followed by a 10-fold serial dilution with sterile PBS. A 100 μL aliquot of the diluted suspension was spread evenly onto LB solid medium plates, which were then incubated at 28 °C for 48 h. After incubation, the number of colonies was counted. For the zone of inhibition test, the sample was cut into 10 mm discs, and the bacterial

suspension was diluted to 10^5 CFU·mL^{-1} with PBS. A 100 μL portion of the bacterial suspension was spread onto the surface of an LB agar plate, and the sample discs were placed onto the surface and gently pressed. The plate was incubated at 28 °C for 48 h, and the zone of inhibition was measured and recorded.

For scanning electron microscopy (SEM) analysis, the bacterial suspension was diluted to 10^6 CFU·mL^{-1} with PBS, and the sample was added to achieve a final concentration of 100 mg·mL^{-1}. The mixture was incubated at 28 °C for 24 h. After incubation, the bacterial pellet was collected and rinsed three times with 0.1 mol·L^{-1} phosphate buffer (pH 7.0) for 15 min each. The sample was fixed with 1% osmium tetroxide for 1–2 h, followed by three rinses with 0.1 mol·L^{-1} phosphate buffer. The sample was dehydrated using a gradient of ethanol (30%, 50%, 70%, 80%, 90%, and 95%) for 15 min each, and two treatments with 100% ethanol for 20 min each. After critical point drying, the sample was mounted and observed under an SEM.

2.5. Salt–alkali pretreatment of adsorbents

To fully utilize the unique anti-polyelectrolyte effect of the PVPA–PAO composite hydrogel adsorbent, a salt–alkali pretreatment technique was employed. A salt–alkali solution was prepared by dissolving 11.69 g of NaCl and 0.08 g of NaOH in 100 mL of deionized water. Then, 5 mg of the dry PVPA–PAO membrane sample was immersed in the solution at 80 °C for approximately 2 h, until the hydrogel became transparent and fully swollen. After pretreatment, the hydrogel membranes were collected using a polyester fiber mesh and thoroughly rinsed with deionized water to remove residual salts and alkali, before being stored for subsequent adsorption experiments. The PAO adsorbent samples were pretreated following the same procedure.

2.6. Water diffusion test

A 5 mg (dry weight) sample of the PVPA–PAO and PAO membranes were salt–alkali pretreated until fully swollen. The swollen hydrogel membranes were then removed using a polyester mesh, soaked in deionized water for 5 min, and subsequently transferred into a 5 mol·L^{-1} NaCl solution. After soaking for 5 min, the membranes were taken out, gently wiped to remove surface moisture, and placed on a glass plate. Subsequently, 10 μL of a 0.1 g·L^{-1} Rhodamine B solution was carefully dropped onto the surface of each membrane. After 10 s, the diffusion of the dye across the diameter of the PVPA–PAO and PAO membranes was observed.

2.7. Optimization of pH for uranium adsorption

To evaluate the effect of pH on uranium adsorption, simulated concentrated seawater containing 2 mol·L^{-1} NaCl was prepared to mimic the salinity of concentrated natural seawater. Uranyl nitrate was dissolved in the brine to obtain a final uranium concentration of 8 parts per million (ppm). The pH of the uranium-containing brine was adjusted to 3.0, 4.0, 5.0, 6.0, 7.0, 8.0, and 9.0 using NaOH and HCl solutions. For each pH condition, 5 mg (dry weight) of salt–alkali pretreated adsorbent was added to 1000 mL of the prepared uranium containing simulated concentrated seawater. The adsorption experiments were conducted at 30 °C with continuous shaking at 120 rpm for 48 h. After the adsorption period, the residual uranium concentration in the supernatant was measured using UV-Vis spectrophotometry. A standard calibration curve was constructed using a series of uranium solutions with known concentrations, and the uranium content in each sample was quantified accordingly. The adsorption capacity of the adsorbent was calculated using Eq. (1).

$$q_t = \frac{(C_0 - C_t) \times V}{m} \tag{1}$$

where C_0 (mg·L^{-1}) is the initial uranium concentration, q_t (mg·g^{-1}) is the uranium adsorption after contact time t, V (L) is the volume of uranium-containing simulated concentrated seawater, C_t (mg·L^{-1}) is the uranium concentration at time t, and m (g) is the dry weight of the adsorbent.

2.8. Adsorption kinetics test

To investigate the adsorption kinetics of uranium by PVPA–PAO and PAO, simulated concentrated seawater containing 8 ppm uranium was prepared and adjusted to the optimal adsorption pH of 6.0. A total of 5 mg (dry weight) of salt–alkali pretreated adsorbent was added to 1000 mL of the prepared uranium-containing brine. The adsorption experiment was conducted at 30 °C with continuous shaking at 120 rpm for a total duration of 48 h. Simulated concentrated seawater samples were collected at 2-h intervals until adsorption equilibrium was achieved. The residual uranium concentration in each sample was determined using UV-Vis spectrophotometry.

The adsorption kinetics were analyzed by fitting the experimental data to the pseudo-first-order and pseudo-second-order models, represented by Eqs. (2) and (3), respectively.

$$\ln(q_e - q_t) = \ln q_e - k_1 t \tag{2}$$

$$\frac{t}{q_t} = \frac{1}{k_1 q_e^2} + \frac{t}{q_e} \tag{3}$$

$$\frac{dq_t}{dt} = \frac{k_1 q_e^2}{(1 + t k_1 q_e)^2} \tag{4}$$

where q_e (mg·g^{-1}) is the uranium adsorption capacities at equilibrium; while k_1 (min^{-1}) and k_2 (g·mg^{-1}·min^{-1}) are the corresponding rate constants. The instantaneous adsorption rate (v_t, mg·g^{-1}·min^{-1}) at time t was determined using Eq. (4), which is the first derivative of the pseudo-second-order model (Eq. (3)) with respect to time t.

2.9. Adsorption isotherms

To investigate the adsorption behavior of the adsorbent, isotherm experiments were performed using uranium-containing simulated concentrated seawater at pH 6.0, with initial uranium concentrations ranging from 2 to 128 ppm. A total of 5 mg (dry weight) of salt–alkali pretreated adsorbent was added to 1000 mL of the uranium solution. The adsorption process was conducted at 30 °C with agitation at 120 rpm for 48 h to ensure equilibrium. After equilibrium was reached, simulated brine samples were collected and analyzed for uranium concentration using UV-Vis spectrophotometry. The equilibrium adsorption data were fitted to the Langmuir and Freundlich isotherm models, represented by Eqs. (5) and (6), respectively.

$$\frac{C_e}{q_e} = \frac{C_e}{q_m} + \frac{1}{k_3 q_m} \tag{5}$$

$$q_e = k_4 C_e^{\frac{1}{n}} \tag{6}$$

where C_e (mg·L^{-1}) is the equilibrium concentration of uranium in solution, q_m (mg·g^{-1}) is the theoretical maximum adsorption capacity, k_3 (L·mg^{-1}) is the Langmuir equilibrium constant related to the affinity between the adsorbent and uranium ions, k_4 ((mg·g^{-1})·(L·mg^{-1})$^{1/n}$) is the Freundlich constant indicating adsorption capacity, and n (dimensionless) is the Freundlich intensity parameter reflecting the heterogeneity of the adsorption surface.

2.10. Reusability test

To evaluate the reusability of the adsorbent, the uranium-loaded membrane was subjected to elution using 20 mL of a desorption solution containing 1 mol·L^{-1} Na_2CO_3 and 0.1 mol·L^{-1} H_2O_2. The elution process was conducted at room temperature (approximately 25 °C) for 10 min. After elution, the membrane adsorbent was reused in a subsequent uranium adsorption experiment under the same conditions. The elution efficiency (EE; %) was calculated using Eq. (7) based on the uranium content before and after desorption.

$$EE = \frac{C_{el} \times V_{el}}{(C_0 - C_{ad}) \times V_{ad}} \times 100\% \quad (7)$$

where C_{el} (mg·L^{-1}) is the concentration of uranium in the eluent, V_{el} (L) is the volume of the eluent, C_0 (mg·L^{-1}) is the initial uranium concentration in simulated concentrated seawater, C_{ad} (mg·L^{-1}) is the uranium concentration in simulated concentrated seawater after uranium uptake, and V_{ad} (L) is the volume of the simulated concentrated seawater used for adsorption.

2.11. Adsorption selectivity

To assess the adsorption selectivity of PVPA–PAO toward uranium in the presence of coexisting ions, competitive adsorption experiments were conducted in simulated concentrated seawater. The simulated concentrated seawater was prepared by dissolving appropriate amounts of inorganic salts in a 2 mol·L^{-1} NaCl solution to raise the concentrations of interfering metal ions. The concentrations of U, V, Cr, Mn, Fe, Co, Ni, Cu, Zn, Ba, and Pb were adjusted to 100 times their typical levels found in natural seawater [34,35]. A total of 10 mg (dry weight) of salt–alkali pretreated adsorbent was added to 1000 mL of the prepared mixed-ion simulated concentrated seawater (adjusted to pH 6.0), and the adsorption experiment was carried out at 30 °C with agitation at 120 rpm for 12 h. After equilibrium, the residual concentrations of metal ions were determined by ICP-MS. The adsorption capacities of various ions were calculated to evaluate the selectivity of PVPA–PAO for uranium over competing ions.

2.12. Computational method

Quantum chemical studies are performed using density functional theory (DFT) implemented in GAUSSIAN 16 package [36]. Geometry optimization analysis was calculated at B3LYP hybrid functional [37] with GD3BJ dispersion correlation at 6–31* basis sets for C, H, O, N, and P atoms and SDD basis for U atom [38,39]. Vibrational frequency analysis was computed to ensure the minimum have no imaginary frequency.

3. Results and discussion

3.1. Physicochemical characterization of PVPA–PAO

The PVPA–PAO hydrogel was physically cross-linked through electrostatic interactions between deprotonated PVPA and protonated PAO, resulting in a stable network structure. In aqueous solution, VPA ionized while PAO became protonated. Under the action of an initiator, underwent radical polymerization to generate PVPA, which subsequently cross-linked with protonated PAO to form the hydrogel [40] (Fig. 2(a)). A simplified schematic of the synthesis procedure is presented in Fig. S1 in Appendix A to visually summarize the preparation steps of PVPA–PAO. The presence of characteristic functional groups in the prepared hydrogels was identified by FTIR spectroscopy. As shown in Fig. 2(b), diagnostic bands of the protonated amine ($-NH_3^+$) and phosphonic acid (phosphonate) groups indicate the successful incorporation of these functionalities into the polymer network. The band at ~2900 cm^{-1} is assigned to the N–H stretching of the protonated amine; the band near 1630 cm^{-1} is attributed to the C=N stretching of the amidoxime moiety; the bands at 1250–1200 and 1070–1040 cm^{-1} correspond to the P=O and P–O stretching modes of the phosphonic acid (phosphonate) groups, respectively; and the band at 950–930 cm^{-1} corresponds to the N–O stretching of the amidoxime group. The major FTIR bands and their assignments are summarized in Table S1 in Appendix A. To investigate the functional groups and confirm the chemical structures of the synthesized polymeric adsorbents, Raman spectroscopy was performed on PVPA–PAO and PAO. As shown in Fig. 2(c), characteristic peaks at ~1620 and ~920 cm^{-1}, are corresponding to the C=N stretching and N–OH bending vibrations of the amidoxime groups, respectively. The distinct bands in the range of 1040–1070 and ~950 cm^{-1} are attributed to the P=O stretching and P–OH bending vibrations [41], respectively, indicating the presence of phosphonic acid group. The presence of protonated amine groups is evidenced by a weak broad band around 3200–3400 cm^{-1} (N–H stretching). Additional peaks at ~1250–1350 cm^{-1} correspond to C–N stretching vibrations. The characteristic C–H stretching vibrations appear around 2850–2950 cm^{-1}. These results collectively verify the presence of the target functional groups. The main Raman peaks and their corresponding vibrational mode assignments are summarized in Table S2 in Appendix A.

In addition, X-ray diffraction (XRD) and atomic force microscopy (AFM) has been conducted. The XRD pattern shows a broad diffraction peak around $2\theta \approx 15°–30°$, confirming the amorphous nature of the polymer matrix (Fig. S2 in Appendix A). This indicates that the PVPA–PAO molecular chains exhibit short-range ordering or disordered aggregation. Such an amorphous structure facilitates swelling and structural adaptability during adsorption, thereby enhancing the material's solute uptake capacity. The AFM images reveal a rough surface with granular and protruding structures (Fig. S3 in Appendix A), which increases the specific surface area and provides more adsorption sites, thus enhancing adsorption efficiency. Additionally, the AFM phase images show varying viscoelastic characteristics of the material surface. The viscoelasticity helps the adsorbent adapt to different environmental conditions, such as changes in salinity and temperature, providing a certain degree of structural stability. For instance, in high-salt environments, the viscoelastic properties of PVPA–PAO help maintain good structural integrity and adsorption performance.

The prepared polyelectrolyte hydrogel adsorbent is shown in Fig. S4 in Appendix A. Its mechanical properties were quantified by tensile stress–strain testing. As shown in Fig. 2(d), the PVPA–PAO hydrogel exhibited a fracture stress of ~352 kPa and a fracture strain of ~1158%, whereas the PAO hydrogel showed ~217 kPa and ~793%, respectively. The superior performance of PVPA–PAO arises from the coexisting strong and weak electrostatic interactions between deprotonated phosphonic acid groups and protonated amidoxime groups within the network: the strong ionic interactions function as rigid cross-linking points that increase tensile strength, while the weak ionic interactions act as dynamic, reversible sacrificial bonds that dissipate energy under deformation, thereby enhancing toughness.

In view of the anti-polyelectrolyte effect exhibited by electrostatically cross-linked hydrogels in salt-rich media, a salt–alkali pretreatment strategy was developed. After pretreatment, the PVPA–PAO sample exhibited the most significant swelling, with its area increasing more than six-fold compared with the initial state (Fig. 2(e)). ESEM results revealed that, prior to pretreatment, both PVPA–PAO and PAO adsorbents possessed inherent porous structures, with PVPA–PAO exhibiting relatively larger pore sizes

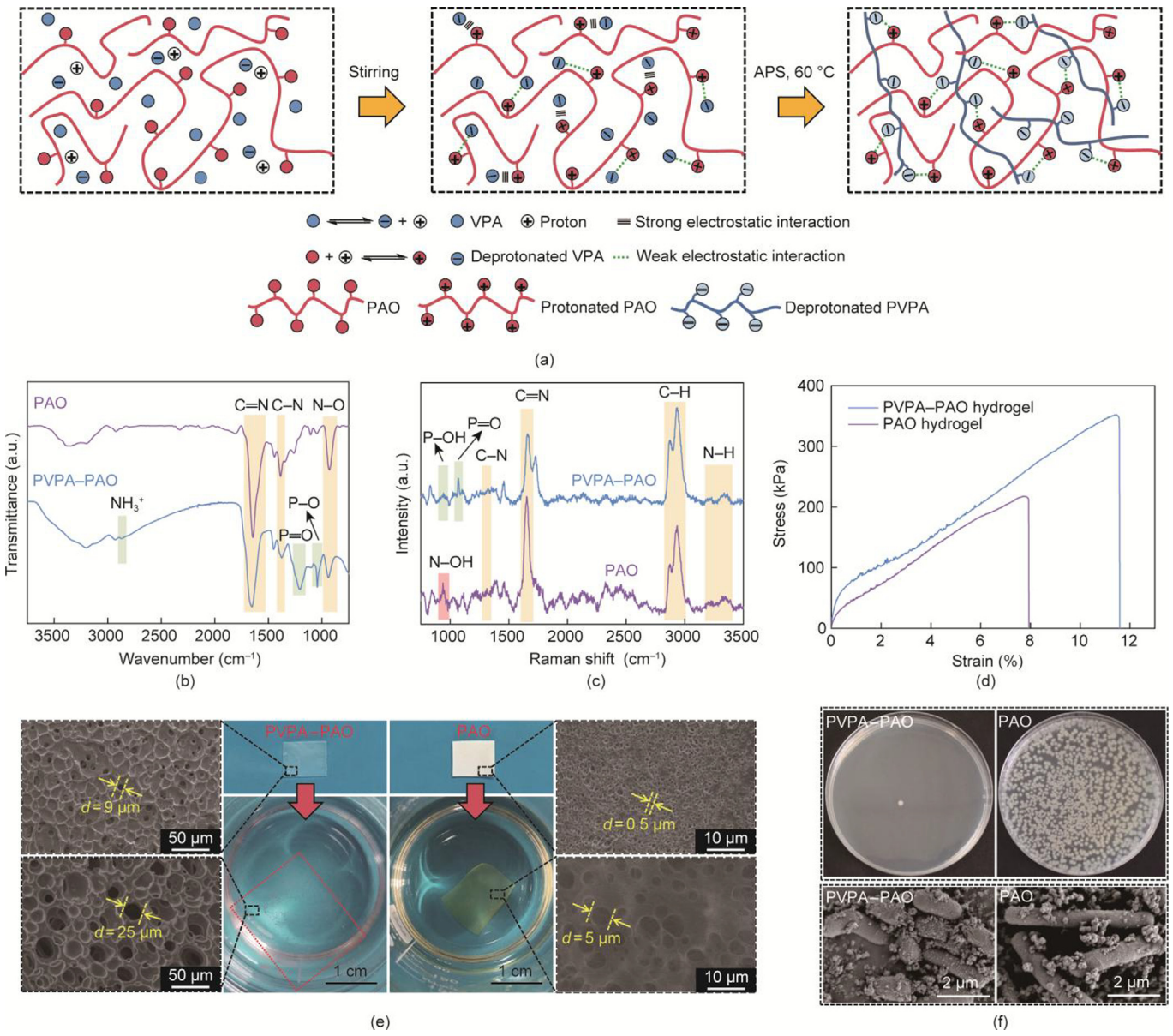

Fig. 2. (a) Schematic illustration of the preparation of PVPA–PAO composite hydrogel adsorbent. (b) FTIR spectra, (c) Raman spectra, and (d) stress-strain curves of PVPA–PAO and PAO hydrogel adsorbents. (e) Physical and SEM images of PVPA–PAO and PAO before and after undergoing salt–alkali pretreatment in salt–alkali solution. (f) Antibacterial activities of the PVPA–PAO hydrogel towards marine bacteria. As a contrast, the antibacterial activities of the pure PAO hydrogel also were tested. a. u.: arbitrary unit.

than PAO. Following salt–alkali pretreatment, the pore sizes of both adsorbents expanded markedly, with PVPA–PAO showing a more pronounced expansion, indicative of the formation of a more open and interconnected porous network. As shown in Fig. S5 in Appendix A, the BET results further confirmed the porous structure of PVPA–PAO, with a specific surface area of 1.54 $m^2 \cdot g^{-1}$ and a total pore volume of 0.004 $cm^3 \cdot g^{-1}$, both slightly higher than those of PAO (1.47 $m^2 \cdot g^{-1}$ and 0.003 $cm^3 \cdot g^{-1}$, respectively). Water contact angle measurements demonstrated the superior hydrophilicity of PVPA–PAO, with the angle decreasing from 40° ± 1° for PAO to nearly 0° for PVPA–PAO due to the highly hydrophilic phosphonic acid groups (Fig. S6 in Appendix A). The combination of enhanced porosity and hydrophilicity is expected to facilitate water penetration and ion transport, thereby improving uranium uptake.

In addition to structural and surface properties, the resistance of adsorbents to biofouling is also critical for maintaining uranium recovery performance in natural seawater. Bacterial adhesion and growth can significantly block adsorption sites and mass transfer channels, resulting in a sharp decline in adsorption efficiency [42]. The antibacterial performance of the adsorbents was therefore investigated. In the antibacterial experiments, the strains we selected were halophilic and salt-tolerant strains obtained by direct culture in concentrated seawater, and their species and abundances are listed in Table S3 in Appendix A. As shown in Fig. 2(f), the plate counting method demonstrated that PVPA–PAO inhibited 99.94% of marine bacterial growth. The antibacterial activity was further supported by inhibition zone assays (Fig. S7 in Appendix A), where a clear zone of 24 mm was observed for PVPA–PAO but absent for PAO. SEM observations confirmed these findings: bacteria on PVPA–PAO appeared irregularly shrunken with roughened, disordered membranes, while those on PAO retained intact rod-like morphologies with smooth membranes. The antimicrobial properties of PVPA–PAO arise from the synergistic action of protonated amino groups and phosphonic acid groups. The

positively charged amino groups disrupt bacterial cell membranes via electrostatic interactions, whereas phosphonic acid groups destabilize the phospholipid bilayer [43,44]. These combined effects cause leakage of intracellular components, loss of cell stability, and eventual cell death, thereby preventing biofouling and ensuring the long-term availability of adsorption sites.

A water diffusion test was conducted to evaluate the permeability of PVPA–PAO and PAO membranes under simulated high-salinity seawater conditions (Fig. 3(a)). After removal from a salt–alkali solution, 10 μL of Rhodamine B dye was gently dropped onto each membrane placed on a flat surface. The dye rapidly diffused through the PVPA–PAO membrane, reaching a diameter of 18.2 mm, whereas the PAO membrane showed a much smaller diameter of 5.8 mm. This difference is attributed to the anti-polyelectrolyte effect in high-salinity conditions. The anti-polyelectrolyte effect of the hydrogel arises when ions from the surrounding medium diffuse into the network and interact with the charged functional groups on the side chains. This interaction weakens the original electrostatic attractions between side chains, increases the interchain spacing, and, at the macroscopic level, manifests as a swelling (volume expansion) of the adsorbent. As illustrated in Fig. 3(b), NaCl–NaOH pretreatment introduces counter-ions and induces partial deprotonation of PVPA–PAO, which screens strong interchain electrostatic attractions and triggers an anti-polyelectrolyte effect, enlarging mesh size and exposing more binding sites. By contrast, the PAO hydrogel undergoes significant shrinkage due to partial screening of electrostatic repulsion by counterions, which limits pore accessibility and mass transport. In Fig. 3(c), PAO collapses under high salinity (salt shrinkage), rendering its interior inaccessible to UO_2^{2+}, whereas PVPA–PAO remains swollen with open pathways, enabling rapid diffusion and cooperative binding at amidoxime and phosphoryl sites.

3.2. Uranium adsorption in simulated concentrated seawater

Solution pH is a critical factor in uranium adsorption performance. The adsorption capacity of PVPA–PAO and PAO was evaluated in simulated concentrated seawater (2 mol·L^{-1} NaCl, 8 ppm U) over a pH range of 3–9. Before evaluating the adsorption performance of the adsorbent, it was pretreated with a salt–alkali solution. The salt–alkali pretreatment was implemented to activate surface functional groups on PVPA–PAO prior to uranium adsorption. Immersion in NaCl–NaOH ① removes loosely bound

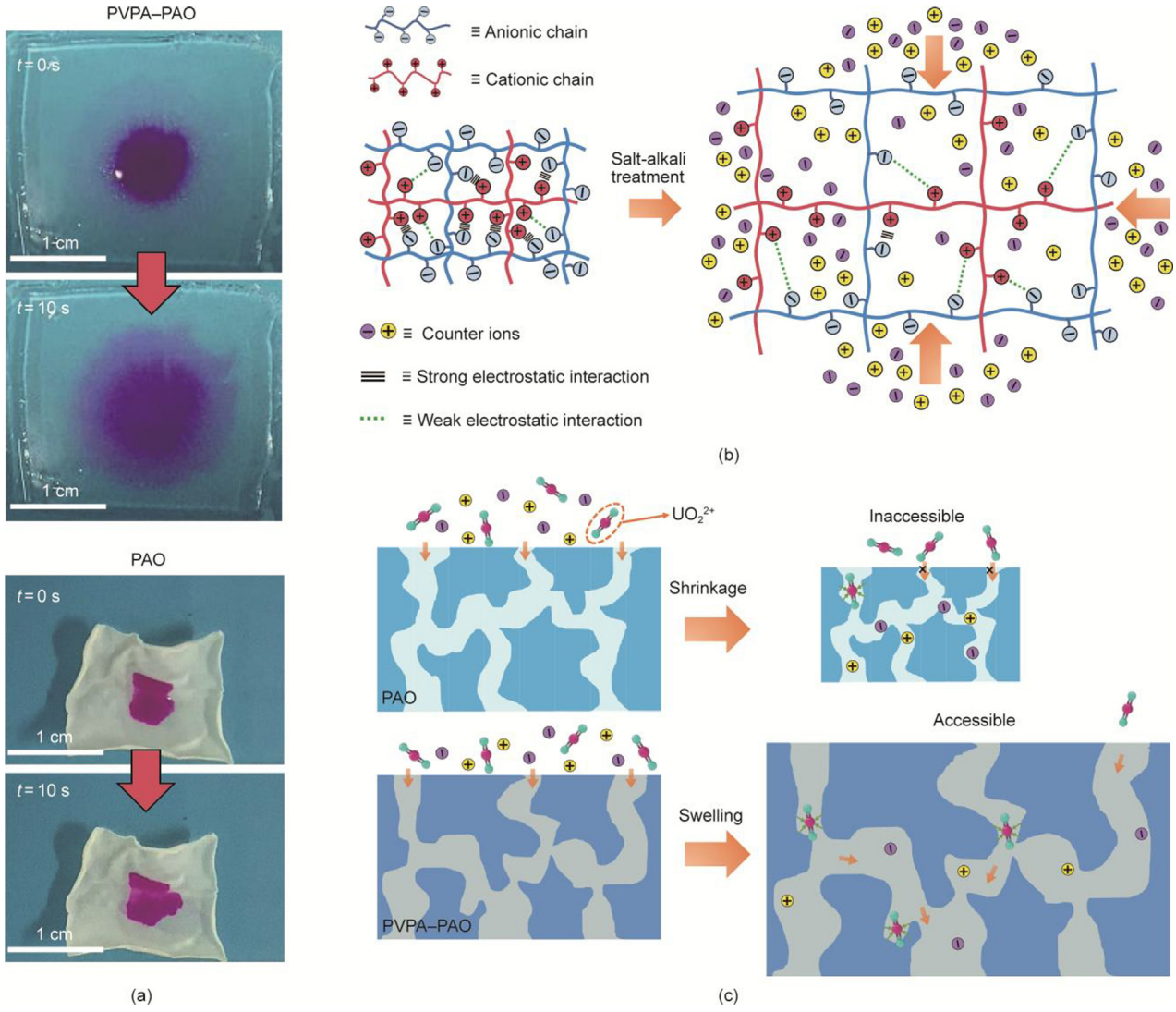

Fig. 3. (a) Permeability test results of PAO and PVPA–PAO membranes after immersion in salt–alkali solution, evaluated by Rhodamine B dye diffusion. (b) Cross-linking and salt-induced swelling mechanism of PVPA–PAO composite hydrogel adsorbent. (c) Schematic diagram for the enhanced adsorption of uranyl ions in concentrated seawater by the PVPA–PAO adsorbent.

impurities and residual acids, ② deprotonates phosphoryl and amidoxime groups to enhance UO_2^{2+} coordination, and ③ provides seawater-like charge screening that causes the material to swell and maintain structural stability in seawater. The results indicated a bell-shaped trend: the adsorption capacity increased with pH up to 6.0, peaking at 820.05 $mg \cdot g^{-1}$, then decreased at higher pH (Fig. 4(a)). At low pH (below 6.0), the positively charged PVPA–PAO surface repels uranyl cations, reducing adsorption [45]. At pH 6.0, uranyl species exist as both cations and anions, allowing for effective electrostatic attraction to the negatively charged surface [46]. This is supported by Zeta potential measurements of PVPA–PAO across the tested pH range (Fig. 4(b)). At higher pH, the dominance of anionic uranyl species leads to repulsion by the negatively charged adsorbent surface, resulting in decreased adsorption. Visual MINTEQ 3.1 was used to speciate U(VI) as a function of pH (Fig. S8 in Appendix A). At low pH (3–5), U(VI) is dominated by free UO_2^{2+} with a small fraction of UO_2Cl^+; adsorption is suppressed because surface functional groups are largely protonated. With increasing pH to mildly acidic or near-neutral conditions, hydrolyzed cationic species emerge, with UO_2OH^+ and $(UO_2)_2(OH)_2^{2+}$ appearing first, and $(UO_2)_3(OH)_5^+$ becoming the major species (~pH 6–7). In this window, partial deprotonation of phosphoryl and amidoxime groups favors coordination with these cationic uranyl species, leading to higher uptake. Around neutral to slightly alkaline pH, minor $(UO_2)_4(OH)_7^+$ and trace $UO_2(OH)_2$ (aqueous solution) are present, and the fraction of anionic complexes begins to rise. At higher pH (> 8), anionic uranyl hydroxo complexes, predominantly $UO_2(OH)_3^-$ with $(UO_2)_3(OH)_7^-$ also pre-

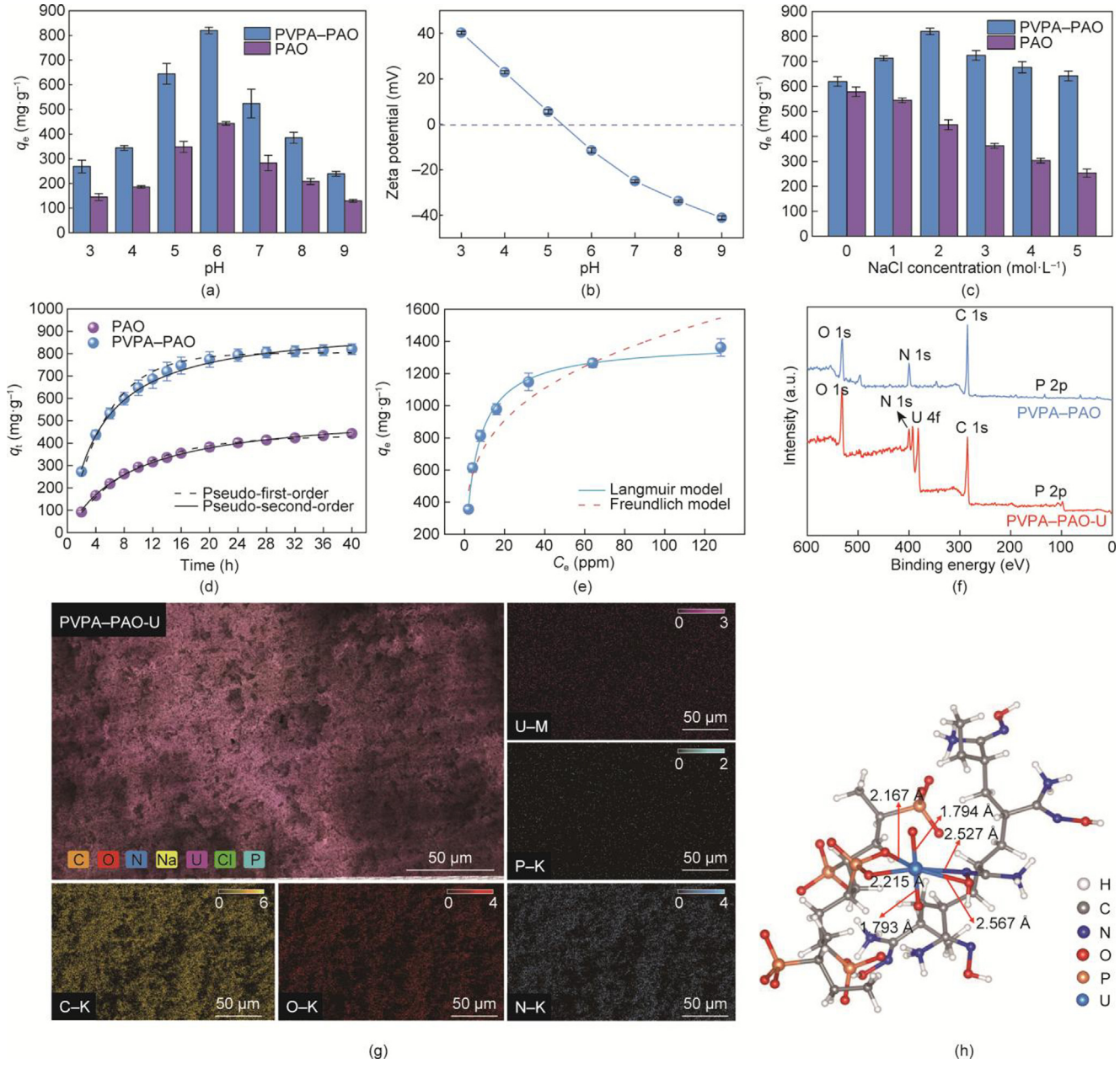

Fig. 4. (a) Adsorption capacities of PVPA–PAO and PAO at different pH values. (b) Zeta potential of PVPA–PAO at pH 3–9. (c) Equilibrium adsorption capacity of PVPA–PAO and PAO in 8 ppm simulated concentrated seawater with different NaCl concentrations. (d) Uranium adsorption kinetics of PVPA–PAO and PAO hydrogel membrane. (e) The equilibrium adsorption isotherms in 8 ppm simulated concentrated seawater at pH 6.0. (f) XPS spectra of PVPA–PAO and PVPA–PAO-U. (g) SEM image and EDS mapping of PVPA–PAO adsorbed with uranium. (h) Schematic diagram of the optimized coordination structure of PVPA–PAO for uranyl ions.

sent, become dominant, resulting in electrostatic repulsion from the negatively charged surface and a decline in adsorption capacity.

To investigate the effect of salinity, a series of uranium solutions (8 ppm U) with varying NaCl concentrations (0, 1, 2, 3, 4, and 5 mol·L^{-1}) were prepared. Since the NaCl concentration in natural seawater is approximately 0.5 mol·L^{-1}, the 1–5 mol·L^{-1} solutions correspond to 2-, 4-, 6-, 8-, and 10-fold concentrated seawater, respectively. Adsorption tests revealed that PVPA–PAO exhibited enhanced adsorption in the 0–2 mol·L^{-1} range, reaching a maximum of 820.05 mg·g^{-1} at 2 mol·L^{-1}. This enhancement can be attributed to the anti-polyelectrolyte behavior of PVPA–PAO, where increasing ionic strength screens the electrostatic attractions between oppositely charged segments of the polymer chains, resulting in an expanded conformation that exposes more phosphoryl and amidoxime groups as active binding sites for UO_2^{2+} ions. In the 2–5 mol·L^{-1} range, a slight decrease in adsorption was observed, which is likely due to the saturation of the anti-polyelectrolyte effect and the excess accumulation of Na^+ ions near the functional groups, partially hindering uranyl coordination. Yet a high capacity of 642.37 mg·g^{-1} was retained even at 5 mol·L^{-1} (Fig. 4(c)). In contrast, traditional PAO adsorbents showed a significant decline in performance with increasing salinity, primarily due to salt-induced shrinkage that inhibits functional group exposure and reduces uranium uptake. Our work leverages the high-salinity environment to achieve enhanced uranium adsorption compared with pure water.

Fig. 4(d) presents the uranium adsorption kinetics of PVPA–PAO and PAO hydrogel membrane adsorbents in 8 ppm uranium solutions under high-salinity conditions (2 mol·L^{-1} NaCl). Adsorption was nearly complete after 24 h, reaching a peak adsorption capacity of 820.05 mg·g^{-1}. In contrast, the sample PAO required more than 36 h to reach saturation adsorption, with lower adsorption capacity of 442.82 mg·g^{-1}. Additionally, the results clearly demonstrate PVPA–PAO accelerated uranium adsorption rate. The fitting of pseudo-first-order and pseudo-second-order kinetic models are presented in Fig. 4(d) and Table S4 in Appendix A. The pseudo-second-order kinetic model yields high correlation coefficients (R^2) of 0.997 and 0.998, indicating excellent agreement with the experimental data and confirming that chemisorption predominantly governs the uranium adsorption process. The adsorption isotherms of PVPA–PAO were determined in high concentration (2 mol·L^{-1}) simulated concentrated seawater with initial uranium concentrations ranging from 2 to 128 ppm (Fig. 4(e)). Both the Langmuir and Freundlich models were applied for fitting analysis. As shown in Table S5 in Appendix A, a superior correlation with the Langmuir model (R^2 = 0.9938) relative to the Freundlich model (R^2 = 0.9097). The process is represented as monolayer adsorption on a homogeneous surface with equivalent sites [47], with each site binding one uranyl ion and interactions between neighboring adsorbed species are negligible. Considering that the adsorption kinetics follow the pseudo-second-order model, it can be concluded that the uranium adsorption process of PVPA–PAO is predominantly governed by monolayer chemisorption on a homogeneous surface.

To elucidate the adsorption mechanism of PVPA–PAO, XPS, EDS, and DFT calculations were carried out. The XPS analysis shows that, after the binding of uranyl ions, the peaks for U $4f_{5/2}$ (392.3 eV) and U $4f_{7/2}$ (381.5 eV) are detected, proving the load of uranium (Fig. 4(f) and Fig. S9 in Appendix A) [48]. Compared with PVPA–PAO, upon U loading the O 1s peak assigned to the amidoxime C=N–O oxygen shifts from 532.8 to 533.0 eV, indicating participation of the amidoxime oxygen in U binding (Fig. S10 in Appendix A). In addition, the phosphonate oxygens shift to higher binding energy (P=O: from 530.6 to 530.7 eV; P–O: from 531.6 to 531.8 eV), further evidencing coordination with UO_2^{2+}. These results are consistent with reduced electron density at the donor oxygens upon complexation. Consistently, the high-resolution N 1s spectra show an increase in the binding energy of the nitrogen in the amidoxime group, corroborating its coordination to UO_2^{2+}. EDS elemental mapping demonstrated uniform distribution of uranium along with C, N, O, and P in the PVPA–PAO matrix (Fig. 4(g)). Visually, the PVPA–PAO adsorbent changed from transparent to orange upon uranium loading (Fig. S11 in Appendix A). The DFT calculations indicate that, in addition to the two axial oxygens of the uranyl ion, the uranium center is coordinated to two oxygen atoms from the phosphonic acid groups (bond lengths: 2.167 and 2.215 Å) and to one oxygen and one nitrogen atom from the amidoxime groups [49] (bond lengths: 2.567 and 2.527 Å), as illustrated in Fig. 4(h). Electron density analysis reveals that the functional oxygen atoms in PVPA and the oxygen and nitrogen atoms in PAO create low-potential regions that attract the positively charged uranyl ion (Fig. S12 in Appendix A).

As reusability is one of the most important indexes to evaluate the economic stability of adsorbents [50], the uranium adsorption capacities of PVPA–PAO were examined after the regeneration reusability process. After 5 cycles, the adsorption capacity could still reach up to 649.64 mg·g^{-1} and the elution rate remained at 83.05% (Fig. 5(a)), suggesting a good reusability [51]. High-concentration sodium carbonate solutions facilitate the desorption of uranium by creating stable uranyl tris-carbonato complexes [$UO_2(CO_3)_3^{4-}$]. When sodium carbonate is used in combination with hydrogen peroxide for uranium elution, it leads to the formation of highly stable uranyl peroxo-carbonato complexes [$UO_2(O_2)(CO_3)_2^{4-}$]. The inclusion of hydrogen peroxide promotes the formation of this complex, which is thermodynamically more stable than the uranyl tris-carbonato complex, exhibiting a stability that is four orders of magnitude higher. This enhanced stability aids in the release of uranyl ions from the adsorbent surface, thereby enabling efficient desorption [52,53]. Adsorption selectivity is a crucial performance parameter for real-world uranium recovery from environments [54]. To evaluate this, PVPA–PAO was tested in ion-doped simulated concentrated seawater containing elevated levels of competing metal ions. The cations were selected because they are representative ions in the marine environment, making them potential competitors for evaluating the selective adsorption performance of PVPA–PAO. The ion concentrations are listed in Table S6 in Appendix A. The adsorbent maintained a high uranium adsorption capacity of 18.73 mg·g^{-1}, demonstrating strong selectivity despite the presence of 100-fold excess concentrations of interfering ions (Fig. 5(b)).

3.3. Uranium extraction from concentrated natural seawater

To further evaluate the extraction performance of the adsorbents in concentrated natural seawater, PVPA–PAO samples were immersed for 24 days in filtered and non-filtered real circulating concentrated seawater system from a salt farm (Fig. 6(a)). The primary components of the concentrated seawater and natural seawater are listed in Table S7 in Appendix A. The uranium concentration in the concentrated seawater was measured to be approximately 32.67 μg·L^{-1}, corresponding to roughly 10× the natural seawater concentration (~3.3 μg·L^{-1}). The inset in Fig. 6(a) shows PVPA–PAO before and after uranium adsorption. After a 24-day uptake period, the adsorbents changed color from white to golden yellow, indicating successful uranium adsorption. The anti-polyelectrolyte-effect of PVPA–PAO facilitates efficient seawater concentrated flow, enabling rapid uranium adsorption. PVPA–PAO reached adsorption equilibrium within approximately 24 days, achieving a capacity of 43.89 mg·g^{-1}, as illustrated in Fig. 6 (b). For the PVPA–PAO membrane, the adsorption capacity in filtered and non-filtered natural seawater is comparable, with values

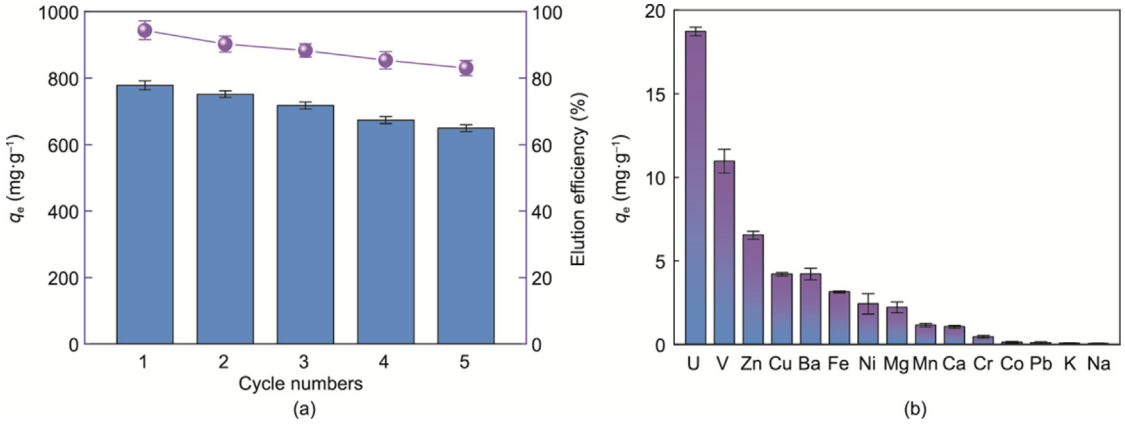

Fig. 5. The reusability and adsorption selectivity. (a) Reusability of PVPA–PAO. (b) Uranium adsorption selectivity of PVPA–PAO in metal ion-doped simulated concentrated seawater.

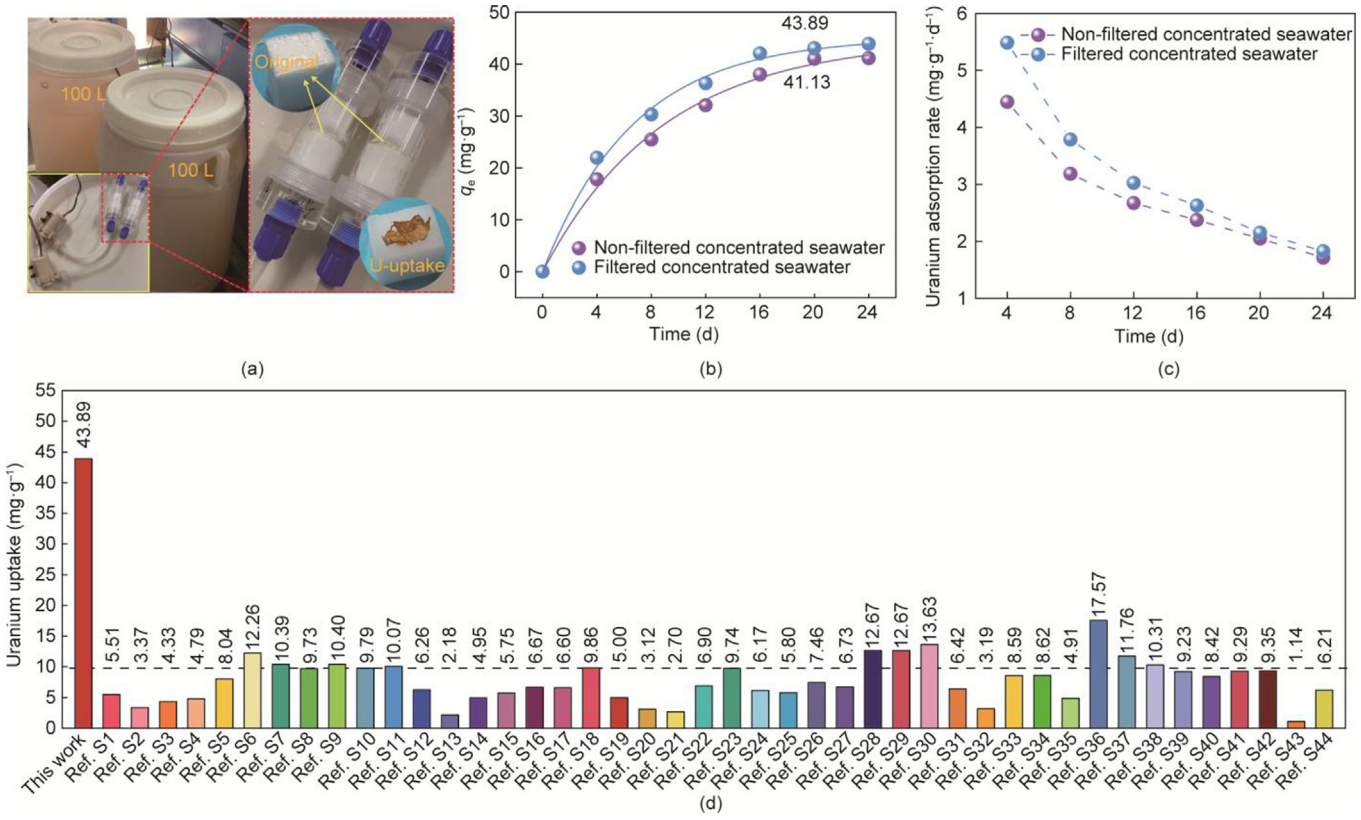

Fig. 6. Uranium extraction from concentrated natural seawater by PVPA–PAO. (a) Schematic of the fluid circulation system used for uranium extraction from real concentrated seawater collected from a salt farm. (b) Adsorption kinetics of uranium extraction from filtered and non-filtered real concentrated seawater. (c) Evolution of the uranium extraction rate as a function of exposure time in concentrated natural seawater. (d) Reported uranium adsorption capacities of amidoxime-based adsorbents in natural seawater conditions. Ref. S1–Ref. S44: references in Appendix A.

of 41.13 mg·g^{-1} for the non-filtered seawater, indicating only a 6.29% decrease in adsorption capacity. The uranium extraction rate over time in concentrated natural seawater is shown in Fig. 6(c). PVPA–PAO achieves an average uranium adsorption rate of 1.83 mg·g^{-1}·d^{-1}. The anti-polyelectrolyte effect of the PVPA–PAO adsorbent not only enhances its uptake capacity but also accelerates the overall adsorption rate. Both the uranium adsorption capacity and rate of PVPA–PAO significantly surpass those of previously reported amidoxime-based adsorbents (Fig. 6(d) and Table S8 in Appendix A).

4. Conclusions

In this study, we developed a PVPA–PAO polyelectrolyte composite hydrogel for efficient uranium extraction from concentrated seawater derived from desalination and solar saltworks. The hydrogel network was physically crosslinked via electrostatic interactions between oppositely charged polyelectrolytes. Benefiting from the anti-polyelectrolyte effect, counterions in concentrated seawater weakened internal electrostatic attractions, leading to chain extension and enhanced exposure of uranyl-

binding sites. The introduction of PVPA significantly improved hydrophilicity and enabled effective contact with uranyl ions. After 24 days of immersion in concentrated natural seawater derived from solar saltworks, the hydrogel achieved a high uranium uptake of 43.89 $mg \cdot g^{-1}$ and an average rate of 1.83 $mg \cdot g^{-1}$ d^{-1}, significantly outperforming conventional PAO-based materials. Furthermore, the hydrogel maintained structural integrity and mechanical stability even under harsh conditions (up to 5 $mol \cdot L^{-1}$ NaCl) and exhibited excellent antibiofouling performance, with only 6.29% performance loss in open concentrated seawater. These findings underscore the potential of PVPA–PAO as a robust and scalable adsorbent for uranium recovery from hypersaline environments. Owing to its hydrogel form and strong antibacterial properties, PVPA–PAO is well suited for engineering-scale deployment and field applications. Beyond addressing key technical barriers, the developed hydrogel also shows great potential for uranium extraction from solar salt and desalination brines, demonstrating excellent adsorption performance, waste valorization, and cost-effectiveness, thereby advancing sustainable and high-value marine resource utilization.

CRediT authorship contribution statement

Hui Wang: Writing – original draft, Funding acquisition, Formal analysis, Conceptualization. **Feng Gao:** Visualization, Validation, Resources, Investigation. **Taohong Xu:** Validation, Investigation, Data curation. **Peng Liu:** Visualization, Investigation, Formal analysis. **Zhanhu Guo:** Visualization, Validation, Investigation. **Guanbing Zhou:** Writing – review & editing, Validation, Project administration, Methodology. **Yihui Yuan:** Writing – review & editing, Supervision, Project administration. **Ning Wang:** Writing – review & editing, Supervision, Project administration, Funding acquisition, Conceptualization.

Declaration of competing interest

The authors declare that they have no known competing financial interests or personal relationships that could have appeared to influence the work reported in this paper.

Acknowledgments

This work was supported by the National Key Research and Development Program of China (2023YFC2809000), the National Natural Science Foundation of China (22422603, 52201315, 22266015, 22327807, U23A20104, and U2167220), the Natural Science Foundation of Hainan Province (225YXQN585), the Hainan Province Science and Technology Special Fund (ZDYF2024SHFZ066), and the Young Elite Scientists Sponsorship Program by Chinese Association for Science and Technology (CAST; 2023QNRC001).

Appendix A. Supplementary data

Supplementary data to this article can be found online at https://doi.org/10.1016/j.eng.2025.11.024.

References

[1] Li G, Sun J, Chen Z, Rui Z. Editorial for the special issue on carbon capture, utilization, and storage. Engineering 2025;48:1–2.
[2] Zhang Y, Xing E, Han W, Yang P, Zhang S, Liu S, et al. Petrochemical industry for the future. Engineering 2024;43:99–114.
[3] Sandwell P, Winchester B, Mittal S, Markides CN, Beath H, Nelson J. Opportunities for decentralised solar power to improve reliability, reduce emissions and avoid stranded assets. Nat Commun 2025;16(1):8061.
[4] Palmer C. Renewable energy seeks boost from floating wind power. Engineering 2024;35:1–3.
[5] Dong D, Guan J, Wang Z, Wang Y. Current status and trends of nuclear energy under carbon neutrality conditions in China. Energy 2025;314:134253.
[6] Zhang S, Chen L, Qu Z, Zhai F, Yin X, Zhang D, et al. Confining Ti-OXO clusters in covalent organic framework micropores for photocatalytic reduction of the dominant uranium species in seawater. Chem 2023;9(11):3172–84.
[7] Hu E, Chen Q, Gao Q, Fan X, Luo X, Wei Y, et al. Cyano-functionalized graphitic carbon nitride with adsorption and photoreduction isosite achieving efficient uranium extraction from seawater. Adv Funct Mater 2024;34(19):2312215.
[8] Xie Y, Liu Z, Geng Y, Li H, Wang N, Song Y, et al. Uranium extraction from seawater: material design, emerging technologies and marine engineering. Chem Soc Rev 2023;52(1):97–162.
[9] Zhong L, Feng X, Zhang Q, Xie X, Luo F. An imidazole-based covalent-organic framework enabling a super-efficiency in sunlight-driven uranium extraction from seawater. Chem Sci 2024;15(28):10882–91.
[10] Kaushik A, Marvaniya K, Kulkarni Y, Bhatt D, Bhatt J, Mane M, et al. Large-area self-standing thin film of porous hydrogen-bonded organic framework for efficient uranium extraction from seawater. Chem 2022;8(10):2749–65.
[11] Wang H, Zhou G, Xu Y, Guo Z, Yuan Y, Wang N. Absorbents for uranium extraction from seawater. SusMat 2025;5(4):e70022.
[12] Qi JX, Gong JW, Zhang CR, Peng ZH, Cai YJ, Liu X, et al. Ocean wave-driven covalent organic framework/ZnO heterostructure composites for piezocatalytic uranium extraction from seawater. Nat Commun 2025;16(1):1078.
[13] Yang L, Qian Y, Zhang Z, Li T, Lin X, Fu L, et al. A marine bacteria-inspired electrochemical regulation for continuous uranium extraction from seawater and salt lake brine. Chem Sci 2024;15(12):4538–46.
[14] Yang L, Kong XY, Wen L, Jiang L. Engineered surface wettability of nanomaterials for efficient uranium extraction from seawater. ACS Nano 2025;19(8):7434–43.
[15] Sun Z, Chen Z, Wang S, Tai X, Wang X. Nuclear energy: where next? Innovation. In press.
[16] Song Y, Hou L, Lan PC, Xing Z, Sun Q, Lv J, et al. Creating electrochemical accessibility in covalent organic frameworks for uranium extraction via electrodeposition. Nat Commun 2025;16(1):7093.
[17] Zhang C, Shi Y, Shi L, Li H, Li R, Hong S, et al. Designing a next generation solar crystallizer for real seawater brine treatment with zero liquid discharge. Nat Commun 2021;12(1):998.
[18] Yu Y, Liu J, Liu Q, Chen R, Yu J, Zhu J, et al. Synergistic enhancement of antibiofouling and uranium extraction from seawater with β-cyclodextrin microcapsules/polyamidoxime porous network membrane. Desalination 2025;608:118808.
[19] Wang H, Zheng B, Xu T, Cao M, Gao F, Zhou G, et al. Macroporous hydrogel membrane by cooperative reaming for highly efficient uranium extraction from seawater. Sep Purif Technol 2022;289:120823.
[20] Yang G, Zhang YY, Zhu QH, Xia X, Pan N, Ma C, et al. Endeavoring a high amidoxime utilization ratio and adsorption capacity for uranium extraction from seawater: a hydrogen bonding reconstruction strategy. Adv Funct Mater 2025;35(22):2425281.
[21] Yang L, Xiao H, Qian Y, Zhao X, Kong XY, Liu P, et al. Bioinspired hierarchical porous membrane for efficient uranium extraction from seawater. Nat Sustain 2022;5(1):71–80.
[22] Cao M, Luo G, Peng Q, Wang L, Wang Y, Zhao S, et al. Poly(amidoxime)/polyzwitterionic semi-interpenetrating network hydrogel with robust salt-shrinkage resistance for enhanced uranium extraction from seawater. Chem Eng J 2024;481:148536.
[23] Luo J, Yu D, Fu K, Fang Z, Zhang X, Xing M. Adsorption-driven interfacial interactions: the key to enhanced performance in heterogeneous advanced oxidation processes. Engineering 2025;47:22–5.
[24] Sun W, Feng L, Zhang J, Lin K, Wang H, Yan B, et al. Amidoxime group-anchored single cobalt atoms for anti-biofouling during uranium extraction from seawater. Adv Sci 2022;9(10):2105008.
[25] Cui WR, Li FF, Xu RH, Zhang CR, Chen XR, Yan RH, et al. Regenerable covalent organic frameworks for photo-enhanced uranium adsorption from seawater. Angew Chem Int Ed 2020;59(40):17684–90.
[26] Luo G, Ma Y, Cao M, Feng L, Ai J, Zhang J, et al. Salt-shrinkage resistant poly (amidoxime) adsorbent for improved extraction of uranium from seawater. Chem Eng J 2023;464:142569.
[27] Shi S, Meng S, Zhao P, Xiao G, Yuan Y, Wang H, et al. Underwater adhesion and curing of superhydrophobic coatings for facile antifouling applications in seawater. Compos Commun 2023;38:101511.
[28] Yuan Y, Guo X, Feng L, Yu Q, Lin K, Feng T, et al. Charge balanced anti-adhesive polyacrylamidoxime hydrogel membrane for enhancing uranium extraction from seawater. Chem Eng J 2021;421:127878.
[29] Wang H, Xu T, Zheng B, Cao M, Gao F, Zhou G, et al. Cuttlefish ink loaded polyamidoxime adsorbent with excellent photothermal conversion and antibacterial activity for highly efficient uranium capture from natural seawater. J Hazard Mater 2022;433:128789.
[30] Liu S, Tao B, Zuo B, Zheng K, Abdelfattah W, Bao J, et al. Function-oriented design principles for adsorbent materials of uranium extraction from seawater. Chem Eng J 2024;500:156783.
[31] He Y, Hou G, Lu X, Chang P, Shao D. Application of poly(vinylphosphonic acid) modified poly(amidoxime) in uptake of uranium from seawater. RSC Adv 2022;12(7):4054–60.

[32] Zheng SY, Zhou J, Si M, Wang S, Zhu F, Lin J, et al. A molecularly engineered zwitterionic hydrogel with strengthened anti-polyelectrolyte effect: from high-rate solar desalination to efficient electricity generation. Adv Funct Mater 2023;33(43):2303272.
[33] Zheng SY, Mao S, Yuan J, Wang S, He X, Zhang X, et al. Molecularly engineered zwitterionic hydrogels with high toughness and self-healing capacity for soft electronics applications. Chem Mater 2021;33(21):8418–29.
[34] Yan B, Ma C, Gao J, Yuan Y, Wang N. An ion-crosslinked supramolecular hydrogel for ultrahigh and fast uranium recovery from seawater. Adv Mater 2020;32(10):1906615.
[35] Zhou Q, Cao X, Zhang J, Li Y, Du X, Ma Y, et al. Protein with twin binding sites for uranium extraction from seawater. Natl Sci Rev 2025;12(5):nwaf126.
[36] Frisch MJ, Trucks GW, Schlegel HB, Scuseria GE, Robb MA, Cheeseman JR, et al. Gaussian 16, revision C. 01 normal name order, Gaussian 2016.
[37] Stephens PJ, Devlin FJ, Chabalowski F, Frisch MJ. *Ab initio* calculation of vibrational absorption and circular dichroism spectra using density functional force fields. J Phys Chem 1994;98(45):11623–7.
[38] Check CE, Faust TO, Bailey JM, Wright BJ, Gilbert TM, Sunderlin LS, et al. Addition of polarization and diffuse functions to the LANL2DZ basis set for p-block elements. J Phys Chem A 2001;105(34):8111–6.
[39] Hay PJ, Wadt WR. *Ab initio* effective core potentials for molecular calculations. Potentials for K to Au including the outermost core orbitals. J Chem Phys 1985;82(1):299–310.
[40] Zhou G, Yang L, Li W, Chen C, Liu Q. A regenerable hydrogel electrolyte for flexible supercapacitors. iScience 2020;23(9):101502.
[41] Jiang F, Kaltbeitzel A, Zhang J, Meyer WH. Nano-spheres stabilized poly(vinyl phosphonic acid) as proton conducting membranes for PEMFCs. Int J Hydrogen Energ 2014;39(21):11157–64.
[42] Sun Z, Chen Z, Tai X, Wang X. Uranium extraction from seawater: methods and challenges. Sci China Chem 2025;68(9):3923–6.
[43] Skibinska M, Warowicka A, Crousse B, Cytlak T. Synthesis and antibacterial activity of novel phosphonated CF3-β-lactams. ACS Omega 2025;10(17):18062–72.
[44] Li D, Bheemanaboina RRY, Battini N, Tangadanchu VKR, Fang XF, Zhou CH. Novel organophosphorus aminopyrimidines as unique structural DNA-targeting membrane active inhibitors towards drug-resistant methicillin-resistant staphylococcus aureus. MedChemComm 2018;9(9):1529–37.
[45] Zhou G, Chen J, Gao F, Wang H, Yuan Y, Wang N. Thick hydrogel membrane with macro-channel for rapid uranium extraction from seawater. Adv Funct Mater 2025;35(25):2425151.
[46] Ai J, Feng L, Zhang J, Cao X, Luo G, Yuan Y, et al. Hierarchically self-supporting porous ultrathin films with aligned photothermal nanosheets for ultrafast uranium extraction from seawater. Chem Eng J 2024;498:155754.
[47] Wang H, Yao W, Yuan Y, Shi S, Liu T, Wang N. Yeast-raised polyamidoxime hydrogel prepared by ice crystal dispersion for efficient uranium extraction from seawater. Adv Sci 2024;11(17):2306534.
[48] Zhao S, Feng T, Feng L, Yan B, Sun W, Luo G, et al. Rapid recovery of uranium with magnetic-single-molecular amidoxime adsorbent. Sep Purif Technol 2022;287:120524.
[49] Yuan Y, Yu Q, Cao M, Feng L, Feng S, Liu T, et al. Selective extraction of uranium from seawater with biofouling-resistant polymeric peptide. Nat Sustain 2021;4(8):708–14.
[50] Gao P, Hu Y, Shen Z, Zhao G, Cai R, Chu F, et al. Ultra-highly efficient enrichment of uranium from seawater via studtite nanodots growth–elution cycle. Nat Commun 2024;15(1):6700.
[51] Zhou G, Gao F, Liu T, Shi S, Wang H, Yuan Y, et al. Polyamidoxime-coated coconut haustorium derived magnetic biochar adsorbent with photothermal conversion for highly efficient uranium recovery from nuclear wastewater. Adv Funct Mater 2024;34(41):2406329.
[52] Zhang W, Xu C, Che X, Wang T, Willför S, Li M, et al. Encapsulating amidoximated nanofibrous aerogels within wood cell tracheids for efficient cascading adsorption of uranium ions. ACS Nano 2022;16(8):13144–51.
[53] Li H, Li L, Wen J, Ye G, Chen J, Wang X. Introducing self-assembly effect in adsorption process for efficient uranium extraction by zwitterion highly-functionalized fibers. Chem Eng J 2023;456:140935.
[54] Zhao S, Feng T, Zhang J, Cao M, Feng L, Ma Y, et al. Coordination-induced magnetism strategy for highly selective and efficient uranium separation. Adv Sci 2024;11(48):2408642.